



1 **A functional tool to explore the reliability of micro-earthquake focal**  
2 **mechanism solution for seismotectonic purposes**

3

4 **Guido Maria Adinolfi <sup>1\*</sup>, Raffaella De Matteis <sup>1</sup>, Rita De Nardis<sup>2</sup> and Aldo Zollo <sup>3</sup>**

5

6 <sup>1</sup> **Dipartimento di Scienze e Tecnologie, Università del Sannio Via dei Mulini, 59/A, 82100 Benevento,**  
7 **Italy**

8 <sup>2</sup> **Dipartimento di Scienze Psicologiche, della Salute e del Territorio, Università di Chieti-Pescara “G.**  
9 **d’Annunzio”, Via dei Vestini, 32, 66100, Chieti, Italy**

10 <sup>3</sup> **Dipartimento di Fisica, Università di Napoli “Federico II”, Complesso Universitario di Monte S. Angelo,**  
11 **via Cinthia, 80124 Napoli, Italy**

12

13 **\* Corresponding author: [gadinolfi@unisannio.it](mailto:gadinolfi@unisannio.it)**

14

15

16

17 **ABSTRACT**

18 Improving the knowledge of seismogenic faults requires the integration of geological, seismological,  
19 and geophysical information. Among several analyses, the definition of earthquake focal mechanisms  
20 plays an essential role in providing information about the geometry of individual faults and the stress  
21 regime acting in a region. Fault plane solutions can be retrieved by several techniques operating in  
22 specific magnitude ranges, both in the time and frequency domain and using different data.

23 For earthquakes of low magnitude, the limited number of available data and their uncertainties can  
24 compromise the stability of fault plane solutions. In this work, we propose a useful methodology to  
25 evaluate how well a seismic network used to monitor natural and/or induced micro-seismicity estimates  
26 focal mechanisms as function of magnitude, location, and kinematics of seismic source and consequently  
27 their reliability in defining seismotectonic models. To study the consistency of focal mechanism  
28 solutions, we use a Bayesian approach that jointly inverts the P/S long-period spectral-level ratios and  
29 the P polarities to infer the fault-plane solutions. We applied this methodology, by computing synthetic  
30 data, to the local seismic network operated in the Campania-Lucania Apennines (Southern Italy) to  
31 monitor the complex normal fault system activated during the Ms 6.9, 1980 earthquake. We  
32 demonstrate that the method we propose can have a double purpose. It can be a valid tool to design  
33 or to test the performance of local seismic networks and more generally it can be used to assign an  
34 absolute uncertainty to focal mechanism solutions fundamental for seismotectonic studies.

35

36

37

38

39



40

41 **INTRODUCTION**

42

43 Fault plane solutions represent a primary information that seismologists can retrieve to describe the  
44 earthquake source. The assessment of earthquake location, magnitude and focal mechanism reveals  
45 the fundamental operations to characterize the earthquake source through the point source  
46 approximation. After the earthquake location, origin time and dimension are identified, the focal  
47 mechanism describes the basic geometry and kinematics of a point source in terms of strike, dip and  
48 rake of fault plane along which the earthquake occurred. So, the focal mechanism is the most important  
49 parameter that can be retrieved to recognize the geometry of the seismogenic faults, their style of  
50 faulting and stress regimes active in a region. Moreover, the seismicity and focal mechanisms of events,  
51 also of small magnitudes, are often used to constrain seismotectonic models, individual seismogenic  
52 sources, the regional strain and stress fields. Consequently, an evaluation of their effective reliability  
53 become a fundamental issue in seismotectonic studies.

54 Nevertheless, focal mechanisms cannot be calculated and constrained every time an earthquake occurs.  
55 Although the calculation of focal mechanisms represents a routine analysis inside the seismological  
56 agencies, the solutions are calculated only for a specific range of magnitude, usually greater than 4. In  
57 fact, constraining the solution for earthquakes with small magnitude still represents a challenge, despite  
58 the advancement in the technological process and the use of increasingly performing seismic networks.  
59 This is due to several factors that we will analyse in detail. The techniques used to define the focal  
60 mechanism of large-moderate earthquakes are based on the inversion of the moment tensor, that  
61 corresponds to a stable and robust procedure, so much so that it is the most common method for this  
62 type of analysis (Dreger, 2003; Delouis, 2014; Sokos and Zahradnik, 2013). This technique requires  
63 an accurate knowledge of the propagation medium in relation to the range of frequencies used for the  
64 modelling of the waveforms recorded during an earthquake. The smaller an earthquake, the higher the  
65 frequency range of the signal to be modelled, the more detailed the knowledge and scale of the Earth's  
66 interior must be.



67 Other analytical techniques are based on the recognition of radiation pattern that describes the  
68 earthquake source. According to the position of seismic stations respect to the source, seismic waves  
69 on seismograms show different amplitudes and polarities. These features are employed in a very simple  
70 way by several algorithms to constrain the geometry of the earthquake faulting estimating the angular  
71 parameters strike, dip and rake. The classical method (Raesenberg and Oppenheimer, 1985;) uses the  
72 P-wave polarities, but advanced ones use P- or S- wave amplitudes or amplitude ratios together with  
73 first motions (Snoke, 2003) to better constrain the focal mechanism of small earthquakes. In fact, the  
74 use of polarities alone is not convenient, especially if we consider the micro-seismicity ( $M < 3$ ). The  
75 reasons could be the limited number of available data, their uncertainties and the difficulty to  
76 automatically measure the P-polarity with a sufficient degree of precision. For these reasons, different  
77 techniques using different types of measurements such as P-wave amplitudes (Julian and Foulger, 1996;  
78 Tarantino et al., 2019), P/S or S/P amplitude ratios measured in time or in the frequency domain  
79 (Kisslinger et al., 1981; Rau et al., 1996; Hardebeck and Shearer, 2003; De Matteis et al., 2016), or  
80 S-wave polarizations (Zollo and Bernard, 1991) have been developed. The joint inversion of polarities  
81 and amplitude ratios led to more stable and robust solutions, allowing to account for geological site  
82 effects and to decrease in first approximation the effects produced by the geometric and anelastic  
83 attenuations.

84 Two kinds of errors generally influence the goodness of solution and retrieved model (Michele et al.,  
85 2016). The perturbation errors that are related to how the uncertainty on data affect the model, and  
86 the resolution errors refer to the capability to retrieve a correct model given a dataset as input. In other  
87 words, how accurate could be the model that we can recover, even if error-free data are used. The sum  
88 of perturbation and resolution errors corresponds to the final errors on the model obtained by solving  
89 an inverse problem, as the solution of focal mechanism. In particular, the resolution errors depend on  
90 the available data, and so on the initial condition of the inverse problem. In the case of focal mechanism,  
91 number of seismic stations, as well as seismic network geometry, and velocity structure of the crust  
92 influence the resolution and the reliability of the retrieved model.



93 How will the geometry of a seismic network determine the accuracy of focal mechanism solutions? The  
94 answer to this question is not simple and requires a deep knowledge of geophysical and geological  
95 characteristics of the region, often unrealistic. Moreover, the theoretical relationships that predict the  
96 focal mechanism solutions for an earthquake scenario could be very complicated if several factors, such  
97 as network configuration, noise level, source magnitude or source kinematics are taken into account.  
98 We want to underline that a network configuration may be optimal for earthquake locations, but not for  
99 retrieving fault plane solutions (Hardt and Scherbaum, 1994). In fact, its geometry may resolve some  
100 fault kinematics better than others.

101 A seismic network layout is strictly associated to the goals of the network and to the available funds;  
102 according to these features a network operator decides how many stations are required and where they  
103 should be located (Havskov et al.; 2011). So, the number of seismic stations, the size and geometry of  
104 network are defined after a preliminary phase based on the specific seismological target is evaluated  
105 (Trnkoczy et al., 2009; Hardt and Scherbaum 1994; Steinberg et al. 1995; Bartal et al. 2000). The  
106 number of seismic stations is related also to the dimension of the region to be monitored. Larger  
107 regions require more stations, unless the seismicity target is represented only by strongest earthquakes.  
108 In the case of small earthquakes, the available recordings come from only a portion of the total network,  
109 while the distant stations show a seismic signal buried in the noise. In order to detect and locate low-  
110 magnitude earthquakes, we must increase the number of seismic stations for area unit building a dense  
111 seismic network. Beyond the number of stations that make up a seismic network, it is essential the  
112 number of stations that properly record a seismic event, i.e. that provide not saturated seismic signals  
113 with a high signal-to-noise ratio (Havskov et al.; 2011).

114 In this study, we propose a useful tool to evaluate both 1) the reliability of focal mechanism solutions  
115 inferred by the inversion of different seismological data and 2) the performance of seismic network to  
116 assess focal mechanism solutions and their errors. We evaluate the network capability to solve focal  
117 mechanism as function of magnitude, location, and kinematics of seismic source. We consider three  
118 synthetic data measurements: P-wave polarities, P- S-wave amplitude spectral ratios and polarities and



119 amplitude ratios together. Moreover, different levels of noise are considered in order to simulate more  
120 realistic conditions.

121 We selected as target the Irpinia Seismic Network (ISNet), a local seismic network that monitors the  
122 Irpinia complex normal fault system (Southern Italy), activated during the Ms 6.9 earthquake of 23rd  
123 November 1980. Evaluating the specific performance of an existing network for a seismological goal is  
124 critical and can be used to decide how to improve its layout.

125

## 126 **METHOD**

127 We estimated focal mechanism using BISTROP code (De Matteis et al., 2016) that jointly inverts the  
128 ratio between the P- and S-wave long-period spectral levels and the P-wave polarities according to a  
129 Bayesian approach. BISTROP has the advantage to use different observables for the determination of  
130 fault plane solutions, such as the P/S long-period spectral level ratios or P-wave polarities, individually  
131 or together. The benefits of the use of spectral level ratios are multiples: 1) they can be measured for a  
132 broad range of magnitudes; 2) they can be calculated by automatic procedures without visual  
133 inspection; 3) their estimates do not require to identify the first arrival time with extreme precision, but  
134 only a time window of signal containing P- or S-phase is mandatory and 4) as spectral amplitude ratios,  
135 they can generally be used without the exact knowledge of the geological soil conditions (site effects)  
136 and geometric/anelastic attenuation. Moreover, the joint inversion of amplitude spectral ratios and  
137 polarities led to constrain fault plane solutions reducing the error associated to the estimates of  
138 retrieved parameters. BISTROP solves an inverse problem through a probabilistic formulation leading  
139 to a complete representation of uncertainty and correlation of the inferred parameters.

140 For a double couple seismic source, the radiation pattern depends on fault kinematics and relative  
141 source-station position. In fact, it can be represented as function of 1) strike, dip and rake angles ( $\varphi$ ,  $\delta$ ,  
142  $\lambda$ ) and 2) take-off and azimuth angles ( $i_h$ ,  $\varphi_r$ ). We can define the ratio between P- and S-wave radiation  
143 pattern coefficients as:



144 
$$\frac{\mathcal{R}^P(\phi, \delta, \lambda, i_h, \phi_R)}{\mathcal{R}^S(\phi, \delta, \lambda, i_h, \phi_R)} = \left( \frac{\alpha_s^2 \alpha_r}{\beta_s^2 \beta_r} \right) \frac{\Omega_0^P}{\Omega_0^S} \quad (1)$$

145

146 where  $\Omega_0^P$  and  $\Omega_0^S$  are the long-period spectral level of the P- and S-waves, respectively, and  $\alpha_s, \alpha_r,$   
 147  $\beta_s, \beta_r,$  are the P- and S-wave velocities at the source and at the receiver, respectively. The Equation 1  
 148 derives from the ratios of seismic moment for P- and S-waves defined as (Aki and Richards, 1980):

149

150 
$$M_0 = \frac{4\pi \rho_s^{1/2} \rho_r^{1/2} \alpha_s^{5/2} \alpha_r^{1/2} R' \Omega_0^P}{F \langle |\mathcal{R}_{\theta\phi}^P| \rangle} \quad (2)$$

151 and

152

153 
$$M_0 = \frac{4\pi \rho_s^{1/2} \rho_r^{1/2} \beta_s^{5/2} \beta_r^{1/2} R' \Omega_0^S}{F \langle |\mathcal{R}_{\theta\phi}^S| \rangle} \quad (3)$$

154

155 where  $\rho_s$  and  $\rho_r$  are the medium densities at the source and at the receiver, respectively;  $\langle |\mathcal{R}_{\theta\phi}^{SP}| \rangle$  and  
 156  $\langle |\mathcal{R}_{\theta\phi}^S| \rangle$  are the average P- and S-wave radiation patterns, respectively.  $R'$  is the geometrical spreading  
 157 estimated for a linear variation of velocity with depth (Ben-Menahem and Singh, 1981):

158 
$$R' = \sqrt{\frac{\rho_r \alpha_r}{\rho_s \alpha_s}} \frac{R}{\sin i_h} \quad (4)$$

159 in which  $R$  is the epicentral distance and  $i_h$  is the take-off angle;  $v_s$  and  $v_r$  are the velocity at the source  
 160 and at the receiver to be substituted with  $\alpha$  and  $\beta$  values for the case of P- and S-wave. Thus, using  
 161 the displacement spectra, assuming a given source and attenuation model (Boatwright, 1980), we can  
 162 derive from the signal recorded by a seismic station the ratio of radiation pattern coefficients for P- and



163 S-phases, as well as  $\alpha$ ,  $\beta$ ,  $i_h$ ,  $\varphi_r$  are known from the earthquake location and from the velocity model  
164 used. So, from a theoretical point of view, the spectral amplitude ratios measured at several seismic  
165 stations can be used to retrieve the ratio of radiation pattern coefficients  $\mathcal{R}_{\theta\varphi}^P/\mathcal{R}_{\theta\varphi}^S$  as function of the  
166 source-receiver azimuth and take-off angles.

167 BISTROP jointly inverts the spectral amplitude ratios with the observed P-wave polarities with the aim  
168 of inferring the parameters  $\varphi$ ,  $\delta$ ,  $\lambda$  of the focal mechanism in a Bayesian framework. A posterior  
169 probability density function (PDF), for the vector of model parameter  $\mathbf{m}$  ( $\varphi$ ,  $\delta$ ,  $\lambda$ ) and the vector of  
170 observed data  $\mathbf{d}$ , is defined as:

$$171 \quad q(\mathbf{m}|\mathbf{d}) = \frac{f(\mathbf{d}|\mathbf{m})p(\mathbf{m})}{\int_M f(\mathbf{d}|\mathbf{m}')p(\mathbf{m}') d\mathbf{m}'} \quad (5)$$

172

173 where  $f(\mathbf{d}|\mathbf{m})$  is the conditional probability function that represents the PDF given the data  $\mathbf{d}$  and for  
174 parameter vector  $\mathbf{m}$  in the model parameter space  $M$ , and  $p(\mathbf{m})$  is the a priori PDF. If P-wave polarities  
175 and P/S spectral level ratios are independent datasets, the conditional probability function may be  
176 written as:

177

$$178 \quad f(\mathbf{d}|\mathbf{m}) = f(\mathbf{d}^L|\mathbf{m})f(\mathbf{d}^P|\mathbf{m}). \quad (6)$$

179

180 in which the pdf of the data vector  $\mathbf{d}^L$  of  $N^L$  measurements of spectral ratios is multiplied for the pdf  
181 of data vector  $\mathbf{d}^P$  of  $N^P$  measurements of P-wave polarities given the model  $\mathbf{m}$ .

182 Assuming that the observables have the same finite variance, for the  $N^L$  observations of spectral level  
183 ratios the conditional probability function may be defined as:



184 
$$f(\mathbf{d}^L|\mathbf{m}) = \frac{1}{(\sqrt{2\pi}\sigma)^{N_L}} \exp\left(-\frac{\sum_{i=1}^{N_L}\{d_i - [G(\mathbf{m})]_i\}^2}{2\sigma^2}\right) \quad (7)$$

185

186 Where  $G(\mathbf{m})$  represents a functional relationship between model and data and corresponds to Equation  
187 1 and  $\sigma$  represents the uncertainty on the spectral measure.

188 For the  $N^P$  observations of P-wave polarities, the conditional probability function is (Brillinger et al.,  
189 1980):

190 
$$f(\mathbf{d}^P|\mathbf{m}) = \prod_{i=1}^{N_P} \frac{1}{2} [1 + \psi(\mathcal{R}_i^P, \gamma_i, \rho_0) Y_i \text{sign}(\mathcal{R}_i^P)] \quad (8)$$

191

192 in which:

193 .

194 
$$\psi(\mathcal{R}_i^P, \gamma_i, \rho_0) = (1 - 2\gamma_i) \text{erf}(|\rho_0 \mathcal{R}_i^P(\mathbf{m})|) \quad (9)$$

195

196 The quantity reported in square brackets in Equation 8 represents the probability that the observed  $i_{th}$   
197 polarity  $\gamma_i$  is consistent with the theoretical one computed from the model  $\mathbf{m}$ , whose theoretical P-wave  
198 amplitude is  $\mathcal{R}_i^P$  and  $\text{sign}(\mathcal{R}_i^P)$  is its polarity at  $i_{th}$  station for a given fault plane solution. The  
199 parameters  $\rho_s$  and  $\gamma_0$ , referring to the errors in ray tracing due to velocity model ambiguity and to the  
200 uncertainty on polarity reading, regulate the shape of the PDF. For more details about the mathematical  
201 formulation, see De Matteis et al., (2016).

202

203

204





## 205 **Irpinia Seismic Network**

206 Our analysis regards the area of the M 6.9, 1980 Irpinia earthquake (Southern Italy). Since 2005, ISNet,  
207 a local, dense seismic network monitors the seismicity along the Campania-Lucania Apennines covering  
208 an area of about  $100 \times 70 \text{ km}^2$  (Figure 1; Weber et al., 2007). The seismic stations are deployed within  
209 an elliptic area whose major axis, parallel to the Apennine chain, has a NW-SE trend with an average  
210 inter-stations distance of 15 km that reaches 10 km in the inner central zone. Each seismic station  
211 ensures a high dynamic range and it is equipped with a strong-motion accelerometer, Guralp CMG-5T  
212 or Kinematics Episensor, and a short period three-component seismometer, Geotech S13-J with natural  
213 period of 1 sec. In 6 cases, broadband seismometer is installed such as the Nanometrics Trillium with  
214 a flat response in the range 0.025–50 Hz. ISNet is operated by INFO (Irpinia Near Fault Observatory)  
215 and it provides real-time data at local control centres for earthquake early warning systems or real time  
216 seismic monitoring (Satriano et al., 2011). Seismic events are automatically identified and located from  
217 continuous recordings by automatic Earth-worm Binder and data are then manually revised by operators  
218 (Festa et al., 2020).

219 The 1980, M 6.9, Irpinia earthquake was one of the most destructive, instrumental earthquakes of the  
220 Southern Apennines, causing about 3000 fatalities and severe damages in the Campania and Basilicata  
221 regions. It activated a NW-SE trending normal fault system with a complex rupture process involving  
222 multiple fault segments according to (at least) three different nucleation episodes delayed each other  
223 of 20 s (Bernard and Zollo, 1989; Pantosti and Valensise; 1993; Amoruso et al.; 2005). No large  
224 earthquakes occurred in the Irpinia region since 1980. A Mw 4.9 earthquake took place in 1996  
225 originating a seismic sequence inside the epicentral area of the 1980 earthquake (Figure 1; Cocco et  
226 al., 1999). Recent instrumental seismicity occurs mainly in the first 15 km of the crust showing fault  
227 plane solutions with normal and normal-strike slip kinematics, indicating a dominant SW-NE extensional  
228 regime (Pasquale et al., 2009; De Matteis et al., 2012; Bello et al.; 2021). Low-magnitude seismicity  
229 ( $M_L < 3.6$ ) is spread into a large volume related to the activity of major fault segments of the 1980  
230 Irpinia earthquake (Figure 1; Adinolfi et al.; 2019; Adinolfi et al.; 2020). Seismic sequences or swarms



231 often occurred in the area, extremely clustered in time (from several hours to few days) and space and  
232 seem to be controlled by high pore fluid pressure of saturated Apulian carbonates bounded by normal  
233 seismogenic faults (Stabile et al., 2012; Amoroso et al.; 2014).

234

## 235 DATA ANALYSIS

236 We performed a resolution analysis of the reliability of focal mechanisms retrieved by data simulated at  
237 ISNet. The analysis is carried out by evaluating the effect of 1) earthquake magnitude, 2) epicentral  
238 location, 3) earthquake depth, 4) signal-to-noise ratio and 5) fault kinematics. We calculated the  
239 capability of the local network to resolve fault plane solutions using different observables as input data:  
240 a) P-wave polarities, b) P/S spectral amplitude ratios and c) polarities and amplitude ratios together.

241 In order to select focal mechanisms to be used for our resolution study (Figure 2a), we carried out a  
242 statistical analysis to define the most frequent fault plane solutions of instrumental seismicity. We  
243 classified according to the plunge of P- and T-axes the fault plane solutions reported in De Matteis et  
244 al. (2012). The data refer to 2005-2011 seismicity occurred in the Irpinia, excluding those occurred in  
245 Potenza region. As shown in Figure 2b, splitting the range of the data into equal-sized bins, we  
246 selected the focal mechanism corresponding to the most populated class. We report it in Figure 2a as  
247 FM2. This corresponds to normal-strike-slip fault plane solution with strike, dip and rake equal to  $292^\circ$ ,  
248  $53^\circ$  and  $-133^\circ$ , respectively. Then, we decide to test the focal mechanism solution of the 1980 Irpinia  
249 earthquake, a pure normal fault (strike, dip, rake:  $317^\circ$ ,  $59^\circ$ ,  $-85^\circ$ ; Westaway and Jackson; 1987; Fig.  
250 2a) here and after FM1. This solution is very similar to the focal mechanism corresponding to: 1) the  
251 regional stress field (see Supplementary Material); 2) the  $M_L$  2.9, Laviano earthquake, one of the most  
252 energetic earthquakes of the last years (Stabile et al.; 2012), and 3) those of the 2<sup>nd</sup>, 3<sup>rd</sup>, 4<sup>th</sup> bins. Finally,  
253 we selected the solution corresponding to the 5<sup>th</sup> bin reported as FM3 in Figure 2a. This focal  
254 mechanism is quite different from the others due to a predominant component along the fault strike  
255 (strike, dip, rake:  $274^\circ$ ,  $71^\circ$ ,  $-128^\circ$ )



256 For each of three selected fault plane kinematics, we calculated synthetic data (P-wave polarities or P-  
257 and S-wave spectral amplitudes) at seismic stations varying the earthquake location and by using a  
258 local velocity model (Matrullo et al., 2013). We discretize the study area with a square grid (100 X 100  
259 km<sup>2</sup>), centred on the barycentre of ISNet, with 441 nodes and sampling step of 5 km. Each node  
260 corresponds to a possible earthquake epicentre (Figure 3).

261 For each grid node and according to the earthquake magnitude to be tested, we have to select the  
262 ISNet stations for simulations. The number of seismic stations that record an event depends on  
263 earthquake magnitude, source-stations distance, crustal medium properties and on the level of noise.  
264 Theoretical relationships that link the seismic source to the signal recorded at each single station are  
265 quite complicated and are based on the accurate knowledge of crustal volume in which the seismic  
266 waves propagated, such as the three-dimensional wave velocity structure, anelastic attenuation or site  
267 conditions of single receiver. In order to overcome this limitation, we used an empirical relationship to  
268 define the number and the distance of the seismic stations that record a seismic signal as function of  
269 magnitude, once its epicentral location (grid node) and depth are fixed. Using the bulletin data retrieved  
270 by INFO at ISNet during the last two years (January 2019-March 2021; [http://isnet-](http://isnet-bulletin.fisica.unina.it/cgi-bin/isnet-events/isnet.cgi)  
271 [bulletin.fisica.unina.it/cgi-bin/isnet-events/isnet.cgi](http://isnet-bulletin.fisica.unina.it/cgi-bin/isnet-events/isnet.cgi)), we selected two earthquake catalog datasets with  
272 depth equal to 5 (+- 2) km and 10 (+- 2) km, respectively and local magnitude ranging between 1.0  
273 and 2.5. These choices are motivated by the characteristics of the Irpinia micro-seismicity recorded by  
274 ISNet. Then, we divided each dataset in bins of 0.5 magnitude and for each bin we retrieved the median  
275 number of P-wave polarity readings and the median epicentral distance of the farthest station that  
276 recorded the earthquake (Table 1). The bulletin data are manually revised by operators, and we selected  
277 only seismic records that provide P- and/or S- wave arrival times. The median value of the distance of  
278 the farthest station is then used to select the seismic stations for which synthetic data are calculated.  
279 We run simulations only for earthquake recorded at least by 6 seismic stations. The synthetic P-wave  
280 polarities are simulated only at a number of stations corresponding to the median value previously  
281 defined. (Table 1). We pointed out that the number of P-wave polarities empirically assigned is related



282 to the available earthquake catalogue data of the Irpinia region where the seismicity can occur in  
283 different portions of area covered by the network, not always with an optimal azimuthal coverage.  
284 Additionally, we simulated the uncertainty on the measure of spectral level ratios or the effect of seismic  
285 noise adding a gaussian noise to the synthetic data with two different percentage levels, as 5% and  
286 30%.

287

288 With this configuration, we simulated:

289

- 290 • Three datasets of seismic observables: P-wave polarities (D1), P/S spectral level ratios (D2) and  
291 polarities and P/S spectral level ratios together (D3)
- 292 • Two hypocentre depths: 5 km and 10 km
- 293 • Three magnitude bins:  $M_L$  1.0 - 1.5 (M1),  $M_L$  1.5 - 2.0 (M2) and  $M_L$  2.0 - 2.5 (M3)
- 294 • Three fault plane solutions: FM1 (317°, 59°, -85°), FM2 (292°, 53°, -133°) and FM3 (274°, 71°,  
295 -128°)
- 296 • Two level of gaussian noise: 5% and 30%

297

298

## 299 **DISCUSSION**

300 In order to evaluate the seismic network capability to resolve fault plane solutions, we defined five kinds  
301 of map to study how the focal mechanism (FM) resolution and error spatially change in the area where  
302 ISNet is installed:

303

- 304 • Kagan angle misfit map (KAM)
- 305 • Map of the focal mechanism parameter misfit (FMM)
- 306 • Strike, Dip and Rake error map (FME)
- 307 • Kagan angle average map (KAA)



- 308 • Kagan angle standard deviation map (KAS)

309

310 The Kagan Angle (KA) measures the difference between the orientations of two seismic moment tensors  
311 or two double couples. It is the smallest angle needed to rotate the principal axes of one moment tensor  
312 to the corresponding principal axes of the other (Kagan et al.; 1991; Tape and Tape; 2012). The smaller  
313 the KA between two focal mechanisms, more similar they are. In KAM map, for each node the value of  
314 KA between the theoretical and retrieved solution is reported, while in FMM map, the absolute value of  
315 the misfit between the strike, dip and rake angles of the retrieved and theoretical solution is indicated.  
316 FME is defined as the error map of strike, dip and rake in which the uncertainties (standard deviations)  
317 are calculated considering all the solutions with probability larger than the 90% (S90) of the maximum  
318 probability, corresponding to the best solution retrieved. Additionally, these solutions are used to study  
319 how constrained is the FM solution. In fact, the KA is calculated between each FM of S90 solutions and  
320 the retrieved best solution. The mean and the standard deviation of resulting KA distribution are plotted  
321 in KAA and KAS maps, respectively. The smaller KA mean and std, the more constrained is the obtained  
322 fault plane solution.

323 We consider the FM1, i.e. the focal mechanism of the 1980 Irpinia earthquake located at 10 km depth,  
324 first. Looking at Figures 4 and 5, we see the effect of using the three different datasets. Considering  
325 D1, we can calculate the FM only for earthquakes with magnitude 2.0-2.5 for which at least 6 polarities  
326 are available. As shown by KAM map in Figure 4a, the retrieved solutions are characterized by high KA  
327 ( $> 50^\circ$ ) with limited areas or single nodes with values in the range  $40^\circ$ - $50^\circ$ . Therefore, D1 is not  
328 sufficient to retrieve with acceptable accuracy the FMs for earthquakes with magnitude 2.0-2.5. The  
329 same result is obtained for FM2 and FM3 (Figure 4b-c). Comparing the results of the simulations using  
330 D2 and D3 (Figure 5), the accuracy of retrieved solution is improved when P-wave polarities data are  
331 added to spectral level ratios. In fact, the areas in KAM map with high value of KA ( $KA \geq 18^\circ$ ; red or  
332 green areas) disappear or are strongly reduced. Nevertheless, we want to underline that, even with D2  
333 dataset, except in some small areas, the FMs are well retrieved for all magnitudes with the KA misfit  
334 mostly lesser than  $10^\circ$ . The spatial resolution of the network is strongly influenced by the earthquake



335 magnitude. In fact, for both M1 and M2, there are nodes (white areas with  $KA = -1$ ) for which the FMs  
336 cannot be calculated because a minimum number of stations (at least 6) are not available (Table 1). At  
337 the same time, the areas better resolved correspond to the region inside the network, although with  
338 D2 and D3 acceptable solutions are calculated for M1 and M2 earthquakes also outside the network,  
339 (Figure 5).

340 Looking at Figure 6, using the D3 dataset, we observe that, among the FM parameters, the dip angle  
341 is the best resolved compared with strike and rake angles. Considering M2 and M3 focal mechanisms,  
342 the misfit of dip is very low ( $< 8^\circ$ ), followed, in ascending order, by rake and strike that show higher  
343 values ( $10^\circ < \text{misfit} < 22^\circ$ ). For M1 (Figure 6a-d-g), rake and strike misfits are larger than  $50^\circ$ , with  
344 rake worse resolved than strike. The unresolved areas correspond to the regions outside the seismic  
345 network.

346 The KAA and KAS maps (Figures 7 and 8) show how the network constrains the fault plane solution as  
347 function of the epicentral location. Moreover, the Figures 7d-e-f and 8d-e-f indicate that the areas with  
348 KA mean and std greater than  $30^\circ$  and  $20^\circ$ , respectively, are reduced when P-wave polarities and  
349 spectral level ratios data are used. On contrary, only for M1 focal mechanisms there is no improvement  
350 because the number of P-wave polarities is the same for both D2 and D3 datasets (Table 1). The worst  
351 constrained regions correspond to a belt surrounding the seismic network, with KA mean  $< 30^\circ$  and  
352 KA std  $< 20^\circ$  for M2 and M3 solutions. For M1, areas with high uncertainty remain outside and inside  
353 the network, specifically in central and in the eastern sectors.

354 Looking at the uncertainties of FM parameters, obtained by using the D3 dataset, the Figure 9 shows  
355 that the dip is the better constrained parameter with an error  $< 10^\circ$ , also for M1 solutions. The rake  
356 angle shows an uncertainty lesser than  $20^\circ$  for M2 and M3, while it overcomes  $50^\circ$  for M1. The strike  
357 angle reveals the highest uncertainty, with values greater than  $50^\circ$  in the eastern and southern sectors  
358 of the map for all analysed magnitudes (M1, M2 and M3). Accuracy improves moving from M1 to M3  
359 earthquakes.

360 As shown in Figure 10, the accuracy of fault plane solutions, in terms of KA misfit calculated by using  
361 the D3 dataset, is similar for FM1, FM2 and FM3, mostly with values lesser than  $8^\circ$  for all the



362 magnitudes M1, M2 and M3. FM2 and FM3 show a slightly higher precision than FM1 in the area inside  
363 the seismic network (see FMM, FME, KAA and KAS maps for FM2 and FM3 in Supplementary Material).  
364 In the regions outside the network, where the azimuthal gap increases, the FMs better constrained in  
365 descending order are: FM3, FM2 and FM1. This effect should be due to geometric relationship between  
366 the spatial distribution of the seismic stations and the orientation of the principal axes (P, T, B) that  
367 characterize the FMs.

368 Considering the effect of hypocentre depth, the results achieved for earthquakes at 5 km depth, by  
369 using the D3 dataset, are overall unchanged (Figure 11). We note that the fault plane solutions are  
370 slightly worse resolved due to a smaller number of P-wave polarities available for M2 and M3. The KA  
371 misfit mainly is lesser than  $10^\circ$ , even though the number and the dimension of areas with misfit  $> 20^\circ$   
372 are greater than those obtained considering earthquakes at 10 km depth. Moreover, the dip angle  
373 shows a misfit lower than strike and rake angles for M1, M2 and M3; the accuracy of the retrieved FMs  
374 parameters is mainly lesser than  $8^\circ$ , as shown in Figure 11.

375 Previous analyses are carried out considering by using data affected by 5% gaussian error. In the last  
376 test, we simulated synthetic data adding a 30% gaussian error. As illustrated in Figure 12, FM solutions  
377 show overall larger misfit, in particular the KA inside the seismic network is lesser than  $20^\circ$ . The area  
378 best resolved ( $KA < 8^\circ$ ) is considerably y reduced to a small central portion of the network. This result  
379 indicates that the accuracy of the spectral level ratio estimates is crucial: noisy waveforms with low  
380 signal to noise ratio can critically affect the result of the focal mechanism inversion. So, seismic noise  
381 as well as the number of available stations, variable due to the operational condition, strongly influence  
382 the capability of the seismic network to retrieve fault plane solution. Using the results of our simulations,  
383 we classified the focal mechanism provided by De Matteis et al., (2016) according to a quality code  
384 based on the resolution of fault kinematics (Table 2). In fact, we assigned to focal mechanisms of Irpinia  
385 instrumental seismicity a quality A, B and C for solutions corresponding to FM3, FM2 and FM1  
386 kinematics, respectively. The quality A, B and C correspond to the average value of KA misfit ( $FM1=4.5^\circ$ ,  
387  $FM2=3.1^\circ$ ,  $FM3=2.4^\circ$ ) calculated for M1, M2 and M3 magnitudes using D3 dataset and considering  
388 earthquakes at 10 km depth with 5% gaussian errors.



389

## 390 CONCLUSIONS

391 We studied the focal mechanism reliability retrieved by the inversion of data recorded by ISNet, a local  
392 dense seismic network that monitors the Irpinia Fault System in Southern Italy. Three different datasets  
393 of seismological observables are used as input data for focal mechanism determination: a) P-wave  
394 polarities, b) P/S spectral amplitude ratios and c) joint polarities and amplitude ratios. Starting from  
395 empirical observations, we computed synthetic data for a regular grid of epicentre locations at two  
396 depths (5 and 10 km), for earthquake magnitude in the range 1.0-2.5 and for three focal mechanism  
397 solutions. Two different levels of gaussian error (5% and 30%) are added to the data.

398 Main conclusions can be summarized as follows.

- 399 • The joint inversion of P-wave polarities and P/S spectral amplitude ratios allows to retrieve  
400 accurate FM (KA misfit  $< 8^\circ$ ) also for earthquakes with magnitude ranging between 1.0 and 2.5,  
401 at depth of 5 and 10 km. Due to the low-energy magnitude, the number of P-wave polarities is  
402 not adequate to constrain fault plane solutions.
- 403 • The spatial resolution analysis of ISNet shows that the most accurate FM solutions are obtained  
404 for earthquakes located inside the network with strike, dip and rake misfit  $< 8^\circ$ . Nevertheless,  
405 outside the network or at its borders, acceptable solutions can be calculated even if the  
406 azimuthal coverage is not adequate (especially for M2 and M3 events). This peculiarity is due to  
407 geometrical relationship between the recording seismic stations and the orientation of principal  
408 axes (P, T, B).
- 409 • The geometry of the network allows to well resolve fault plane solutions varying between normal  
410 and normal-strike focal mechanism with mainly strike, dip and rake misfit lesser than  $10^\circ$  for  
411 magnitude range 1.5-2.5. The network resolves slightly better normal-strike fault plane solution  
412 than a pure normal focal mechanism.
- 413 • Among the FM parameters, the dip angle shows the lowest uncertainty. Strike and rake angles  
414 reveal higher errors especially for M 1-1.5 earthquakes in the region outside the seismic network.





415 • Dataset affected by 30% gaussian error provide a worsening in the accuracy of the retrieved  
416 FMs. Although the high error level, the area of well resolved fault plane solutions (KA misfit <  
417 20°) persists in the central part of the network, especially for M2 and M3.

418 The methodology described in this work can be a valid tool to design or to test the performance of  
419 local seismic networks, operated to monitor natural or induced seismicity. Moreover, given a network  
420 configuration, it can be used to evaluate the reliability of FMs that represent a fundamental information  
421 in seismotectonic studies. Although it is a theoretical study, many earthquake scenarios with several  
422 magnitude, locations and noise conditions can be simulated to mimic the real seismicity.

423  
424  
425  
426  
427  
428  
429  
430  
431  
432  
433  
434  
435  
436  
437  
438  
439  
440  
441  
442  
443  
444  
445  
446  
447  
448  
449  
450  
451  
452  
453  
454  
455  
456



457 **REFERENCES**

458

459 Adinolfi, G. M., Cesca, S., Picozzi, M., Heimann, S., & Zollo, A. (2019). Detection of weak seismic sequences  
460 based on arrival time coherence and empiric network detectability: an application at a near fault observatory.  
461 *Geophysical Journal International*, 218(3), 2054-2065.

462

463 Adinolfi, G. M., Picozzi, M., Cesca, S., Heimann, S., & Zollo, A. (2020). An application of coherence-based  
464 method for earthquake detection and microseismic monitoring (Irpinia fault system, Southern Italy). *Journal*  
465 *of Seismology*, 24, 979-989.

466

467 Aki, K., and P. G. Richards (1980). *Quantitative Seismology, Theory and Methods*, W.H. Freeman, San  
468 Francisco.

469

470 Amoroso, O., Ascione, A., Mazzoli, S., Virieux, J., & Zollo, A. (2014). Seismic imaging of a fluid storage in  
471 the actively extending Apennine mountain belt, southern Italy. *Geophysical Research Letters*, 41(11), 3802-  
472 3809.

473

474 Amoroso, A., Crescentini, L., & Scarpa, R. (2005). Faulting geometry for the complex 1980 Campania-  
475 Lucania earthquake from levelling data. *Geophysical Journal International*, 162(1), 156-168.

476

477 Bartal, Y., Somer, Z., Leonard, G., Steinberg, D. M., & Horin, Y. B. (2000). Optimal seismic networks in  
478 Israel in the context of the Comprehensive Test Ban Treaty. *Bulletin of the seismological society of America*,  
479 90(1), 151-165.

480

481 Bello, S., De Nardis, R., Scarpa, R., Brozzetti, F., Cirillo, D., Ferrarini, F., ... & Lavecchia, G. (2021). Fault  
482 Pattern and Seismotectonic Style of the Campania–Lucania 1980 Earthquake (M w 6.9, Southern Italy): New  
483 Multidisciplinary Constraints. *Front. Earth Sci*, 8, 608063.

484

485 Ben-Menahem, A., and S. J. Singh (1981). *Seismic Waves and Sources*, 1108 p, Springer-Verlag, New York.

486

487 Bernard, P., & Zollo, A. (1989). The Irpinia (Italy) 1980 earthquake: detailed analysis of a complex normal  
488 faulting. *Journal of Geophysical Research: Solid Earth*, 94(B2), 1631-1647.

489

490 Boatwright, J. (1980). A spectral theory for circular seismic sources; simple estimates of source dimension,  
491 dynamic stress drop, and radiated seismic energy, *Bull. Seismol. Soc. Am.*, 70 (7), 1–27.

492

493 Brillinger, D. R., A. Udías, and B. A. Bolt (1980). A probability model for regional focal mechanism solutions,  
494 *Bull. Seism. Soc. Am.* 70, 149- 170.

495

496 Cocco, M., Chiarabba, C., Di Bona, M., Selvaggi, G., Margheriti, L., Frepoli, A., ... & Campillo, M. (1999).  
497 The April 1996 Irpinia seismic sequence: evidence for fault interaction. *Journal of Seismology*, 3(1), 105-  
498 117.

499

500 Delouis, B. (2014). FMNEAR: Determination of focal mechanism and first estimate of rupture directivity  
501 using near-source records and a linear distribution of point sources. *Bulletin of the Seismological Society of*  
502 *America*, 104(3), 1479-1500.

503

504 De Matteis, R., Matrullo, E., Rivera, L., Stabile, T. A., Pasquale, G., & Zollo, A. (2012). Fault delineation and  
505 regional stress direction from the analysis of background microseismicity in the southern Apennines, Italy.  
506 *Bulletin of the Seismological Society of America*, 102(4), 1899-1907.

507



- 508 De Matteis, R., Convertito, V., & Zollo, A. (2016). BISTROP: Bayesian inversion of spectral-level ratios and  
509 P-wave polarities for focal mechanism determination. *Seismological Research Letters*, 87(4), 944-954.  
510
- 511 Dreger, D. S., Lee, W. H. K., Kanamori, H., Jennings, P. C., & Kisslinger, C. (2003). Time-domain moment  
512 tensor INverse codel (TDMT-INVC) release 1.1. *International Handbook of Earthquake and Engineering*  
513 *Seismology*, WHK Lee, H. Kanamori, PC Jennings, and C. Kisslinger (Editors), Vol. B, 1627.  
514
- 515 Festa, G., Adinolfi, G. M., Caruso, A., Colombelli, S., De Landro, G., Elia, L., ... & Zollo, A. (2021). Insights  
516 into Mechanical Properties of the 1980 Irpinia Fault System from the Analysis of a Seismic Sequence.  
517 *Geosciences*, 11(1), 28.  
518
- 519 Hardebeck, J., and M. Shearer (2003). Using S/P Amplitude Ratios to Constrain the Focal Mechanisms of  
520 Small Earthquakes, *Bull. Seism. Soc. Am.* **93**, 6, pp. 2434–2444, December 2003.  
521
- 522 Hardt, M., & Scherbaum, F. (1994). The design of optimum networks for aftershock recordings. *Geophysical*  
523 *Journal International*, 117(3), 716-726.  
524
- 525 Havskov, J., Ottemöller, L., Trnkoczy, A., Bormann, P. (2012): Seismic Networks. - In: Bormann, P. (Ed.),  
526 *New Manual of Seismological Observatory Practice 2 (NMSOP-2)*, Potsdam : Deutsches  
527 GeoForschungsZentrum GFZ, 1-65.  
528
- 529 Julian, B. R., and G. R. Foulger (1996). Earthquake mechanisms from linear-programming inversion of  
530 seismic-wave amplitude ratios, *Bull. Seism. Soc. Am.* **86** (4), 972-980.  
531
- 532 Kagan, Y. Y. (1991). 3-D rotation of double-couple earthquake sources. *Geophysical Journal International*,  
533 106(3), 709-716.  
534
- 535 Kisslinger, C., J. R. Bowman, and K. Koch (1981). Procedures for computing focal mechanisms from local  
536 (SV/P) z data, *Bull. Seism. Soc. Am.* **71** (6), 1719-1729.  
537
- 538 Matrullo E., R. De Matteis, C. Satriano, O. Amoroso, and A. Zollo (2013). An improved 1D seismic velocity  
539 model for seismological studies in the Campania-Lucania region (Southern Italy), *Geophys. J. Int.* **195**, Issue  
540 1, pp.460-473, doi: 10.1093/gji/ggt224.  
541
- 542 Michele, M., S. Custódio, and A. Emolo (2014). Moment tensor resolution: case study of the Irpinia Seismic  
543 Network, Southern Italy, *Bull. Seismol. Soc. Am.* **104**, 1348-1357, doi: 10.1785/0120130177.  
544
- 545 Pantosti, D., & Valensise, G. (1990). Faulting mechanism and complexity of the November 23, 1980,  
546 Campania-Lucania earthquake, inferred from surface observations. *Journal of Geophysical Research: Solid*  
547 *Earth*, 95(B10), 15319-15341.  
548
- 549 Pasquale, G., De Matteis, R., Romeo, A., & Maresca, R. (2009). Earthquake focal mechanisms and stress  
550 inversion in the Irpinia Region (southern Italy). *Journal of seismology*, 13(1), 107-124.  
551
- 552 Reasenber, P., & Oppenheimer, D. USGS (1985). FPFIT, FPLOT, and FPPAGE: Fortran computer  
553 programs for calculating and displaying earthquake fault-plane solutions. *US Geol. Surv. Open-File Rept.*  
554 85, 739.  
555
- 556 Satriano, C., Elia, L., Martino, C., Lancieri, M., Zollo, A., & Iannaccone, G. (2011). PRESTo, the earthquake  
557 early warning system for southern Italy: Concepts, capabilities and future perspectives. *Soil Dynamics and*  
558 *Earthquake Engineering*, 31(2), 137-153.  
559



560 Snoke, J. A., Lee, W. H. K., Kanamori, H., Jennings, P. C., & Kisslinger, C. (2003). FOCMEC: Focal  
561 mechanism determinations. *International handbook of earthquake and engineering seismology*, 85, 1629-  
562 1630.  
563  
564 Stabile, T. A., Satriano, C., Orefice, A., Festa, G., & Zollo, A. (2012). Anatomy of a microearthquake sequence  
565 on an active normal fault. *Scientific reports*, 2(1), 1-7.  
566  
567 Steinberg, D. M., Rabinowitz, N., Shimshoni, Y., & Mizrachi, D. (1995). Configuring a seismographic  
568 network for optimal monitoring of fault lines and multiple sources. *Bulletin of the seismological society of*  
569 *America*, 85(6), 1847-1857.  
570  
571 Sokos, E., & Zahradník, J. (2013). Evaluating centroid-moment-tensor uncertainty in the new version of  
572 ISOLA software. *Seismological Research Letters*, 84(4), 656-665.  
573  
574 Tape, W., & Tape, C. (2012). A geometric setting for moment tensors. *Geophysical Journal International*,  
575 190(1), 476-498.  
576  
577 Tarantino, S., Colombelli, S., Emolo, A., & Zollo, A. (2019). Quick determination of the earthquake focal  
578 mechanism from the azimuthal variation of the initial P-wave amplitude. *Seismological Research Letters*,  
579 90(4), 1642-1649.  
580  
581 Trnkoczy, A., Bormann, P., Hanka, W., Holcomb, L. G., & Nigbor, R. L. (2009). Site selection, preparation  
582 and installation of seismic stations. In *New Manual of Seismological Observatory Practice (NMSOP)* (pp. 1-  
583 108). Deutsches GeoForschungsZentrum GFZ.  
584  
585 Weber, E., Iannaccone, G., Zollo, A., Bobbio, A., Cantore, L., Corciulo, M., ... & Satriano, C. (2007).  
586 Development and testing of an advanced monitoring infrastructure (ISNet) for seismic early-warning  
587 applications in the Campania region of southern Italy. In *Earthquake early warning systems* (pp. 325-341).  
588 Springer, Berlin, Heidelberg.  
589  
590 Zollo, A., & Bernard, P. (1991). Fault mechanisms from near-source data: joint inversion of S polarizations  
591 and P polarities. *Geophysical Journal International*, 104(3), 441-451.  
592  
593  
594  
595  
596  
597  
598  
599  
600  
601  
602  
603  
604  
605  
606  
607  
608  
609



610 **TABLES**

611  
612  
613  
614  
615  
616  
617  
618  
619  
620  
621  
622

Depth 5 km	Max Distance (km)	No. P-polarities
<i>M<sub>L</sub> 1.0 -1.5</i>	30	1
<i>M<sub>L</sub> 1.5 - 2.0</i>	49	1
<i>M<sub>L</sub> 2.0 - 2.5</i>	57	4
Depth 10 km	Max Distance (km)	No. P-polarities
<i>M<sub>L</sub> 1.0 -1.5</i>	33	1
<i>M<sub>L</sub> 1.5 - 2.0</i>	40	5
<i>M<sub>L</sub> 2.0 - 2.5</i>	66	6

623 **Table 1** Maximum distance of the farthest triggered seismic station and number of P-wave polarities as  
624 function of earthquake magnitude and depth. The relations, empirically derived, are used for the  
625 earthquake simulations.

626  
627  
628  
629  
630  
631  
632  
633  
634  
635  
636  
637  
638  
639  
640  
641  
642  
643  
644  
645  
646  
647  
648  
649  
650  
651  
652  
653  
654  
655  
656  
657



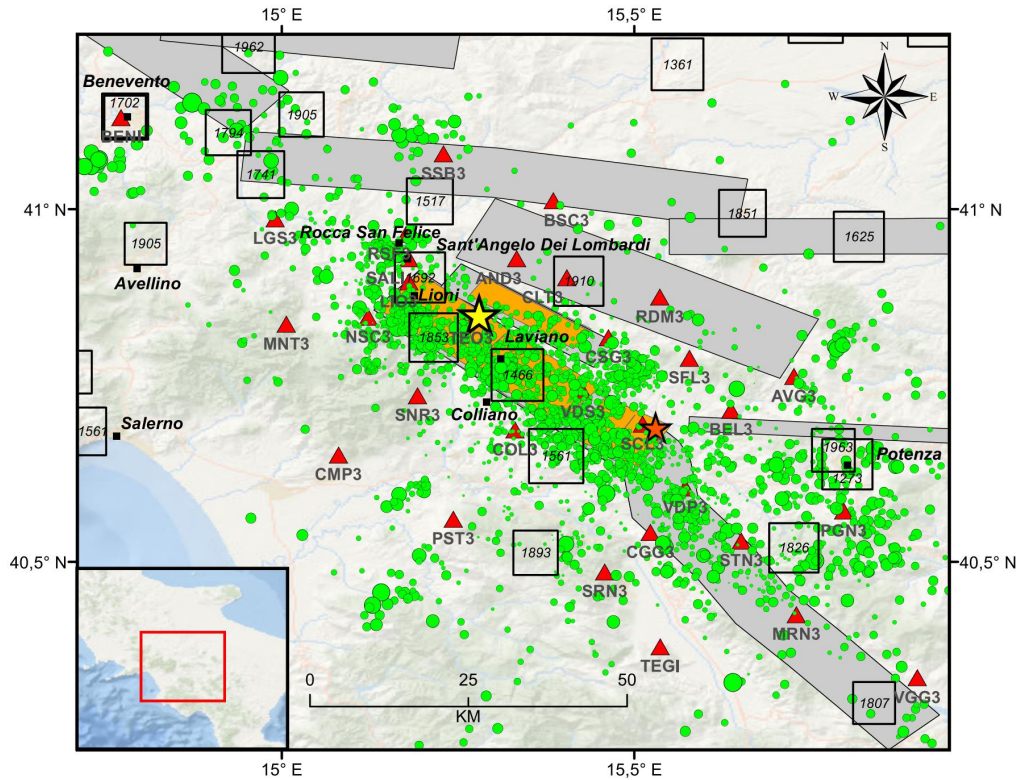
P-plunge (°)	P-trend (°)	T-plunge (°)	T-trend (°)	Strike (°)	Dip (°)	Rake (°)	Quality
55	344	31	196	325	20	-40	A
51	334	36	181	320	15	-30	A
55	14	31	226	355	20	-40	A
53	205	34	49	180	15	-40	A
55	72	33	272	35	15	-50	A
51	177	32	37	290	80	-110	A
54	292	34	91	10	80	-80	A
77	146	9	7	270	55	-100	B
80	235	10	55	325	55	-90	B
76	103	2	6	110	45	-70	B
76	117	2	214	290	45	-110	B
76	82	7	199	275	40	-110	B
75	190	15	10	280	60	-90	B
75	205	15	25	295	60	-90	B
85	230	5	50	140	40	-90	B
83	146	0	53	150	45	-80	B
80	240	10	60	330	55	-90	B
81	233	5	353	270	50	-80	B
81	347	5	227	130	50	-100	B
55	93	10	198	255	45	-140	C
55	133	10	238	295	45	-140	C
48	130	2	38	275	60	-140	C
48	305	2	37	340	60	-40	C
55	202	7	102	345	60	-130	C
58	121	2	27	270	55	-130	C
58	131	2	37	280	55	-130	C
55	342	7	242	125	60	-130	C
47	138	11	36	165	50	-30	C
49	182	14	289	340	45	-150	C
58	151	2	57	300	55	-130	C
49	168	14	61	190	45	-30	C
59	308	15	64	355	65	-60	C
57	306	14	59	115	40	-140	C
57	76	14	189	245	40	-140	C
45	85	6	348	225	65	-140	C
55	22	7	282	165	60	-130	C
57	241	14	354	50	40	-140	C
55	98	7	198	135	60	-50	C
51	115	2	22	145	55	-40	C
55	147	7	47	290	60	-130	C

658  
 659  
 660  
 661  
 662  
 663  
 664  
 665  
 666

**Table 2.** Fault plane solutions of instrumental seismicity occurred in Irpinia region in 2005-2008 and calculated by De Matteis et al., (2012). The solutions are classified according to a quality code based on the resolution of fault plane kinematics as derived in this study. The result of our simulations suggests a quality as follows: FM1=C, FM2=B, FM3=A.

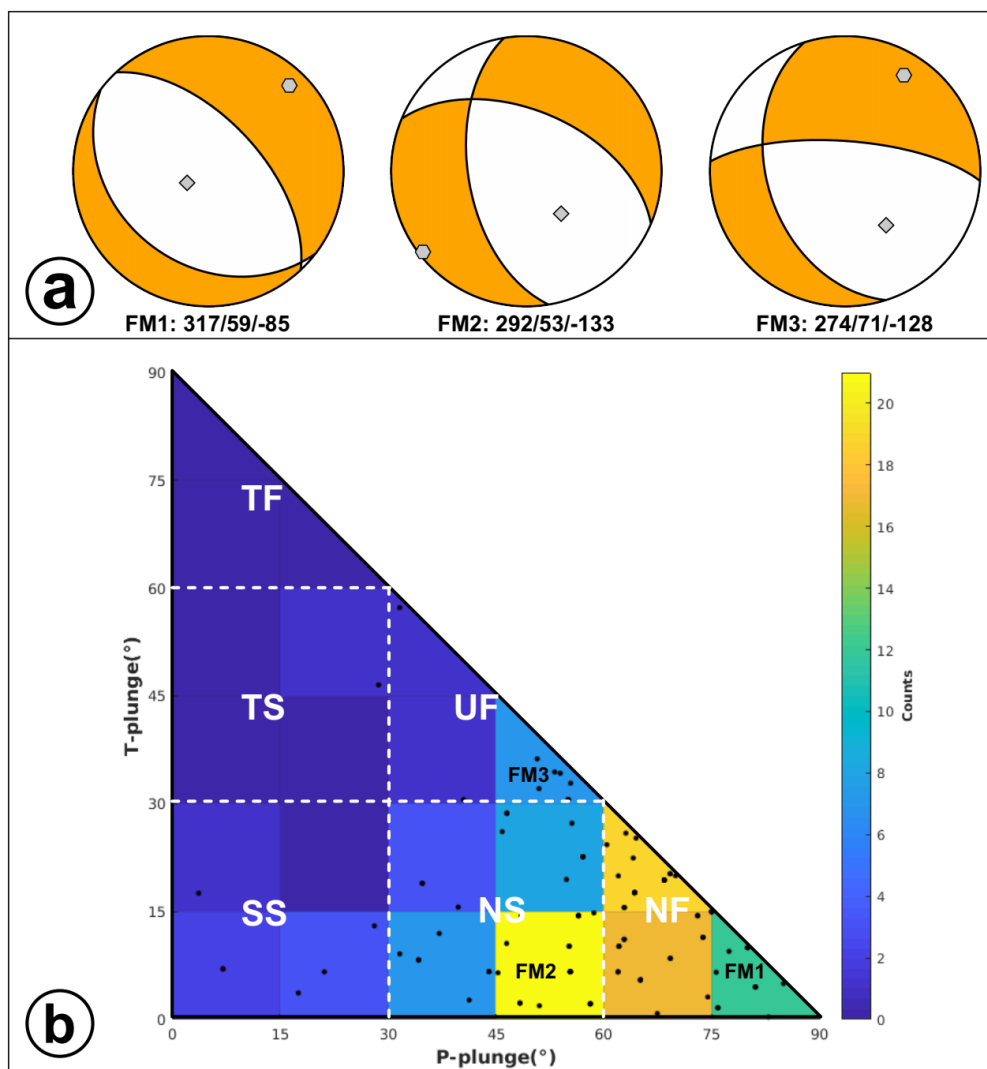


667 FIGURES  
668



669  
670  
671  
672  
673  
674  
675  
676  
677  
678  
679  
680  
681  
682  
683

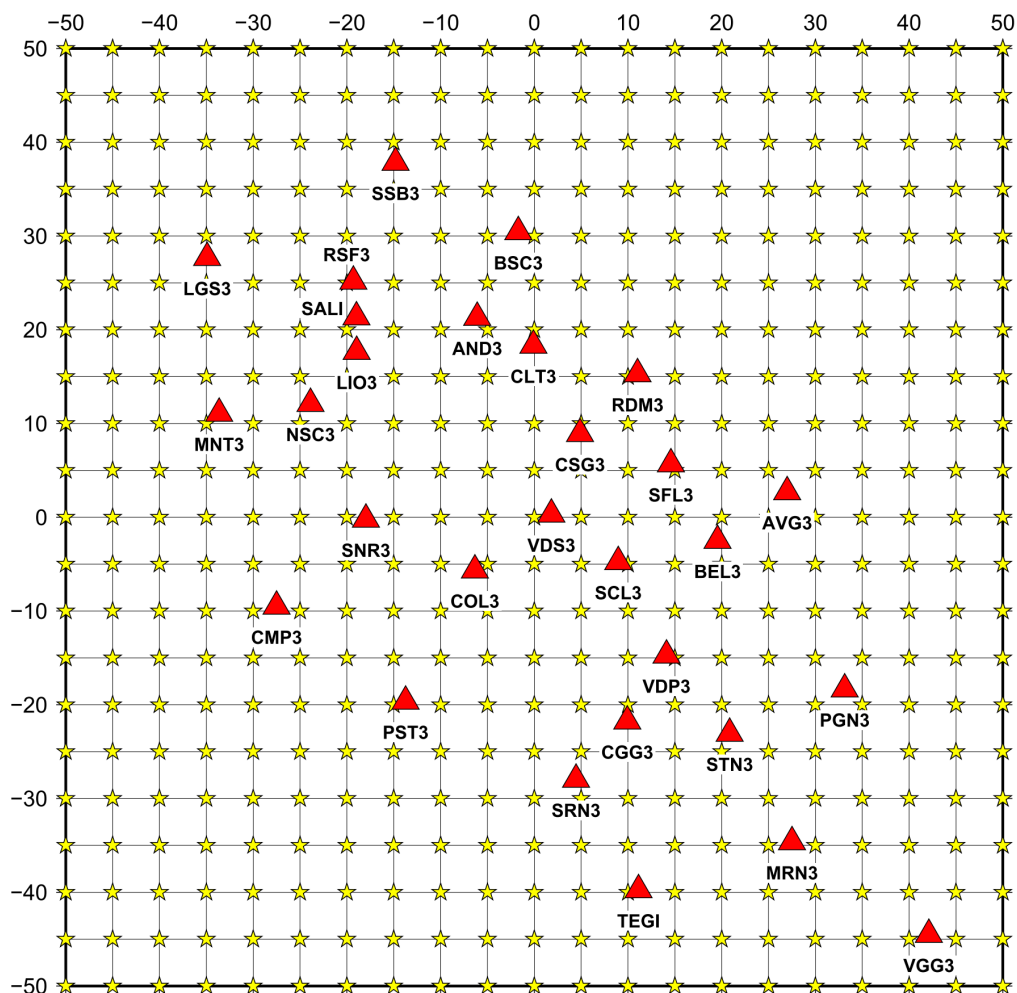
**Figure 1.** Epicentral map of the earthquakes (green circles) recorded by Irpinia Seismic Network (ISNet, red triangles) from 2008 to 2020 (<http://isnet-bulletin.fisica.unina.it/cgi-bin/isnet-events/isnet.cgi>). The yellow and orange stars refer to the epicentral location of the 1980, M 6.9, and of the 1996, M 4.9 earthquakes, respectively. Historical seismicity is shown with black squares ( $I_0 \geq 6-7$  MCS). Seismogenic sources related to the Irpinia fault system are indicated by orange rectangles; potential sources for earthquakes larger than M 5.5 in surrounding areas are indicated in grey (Database of Individual Seismogenic Sources, DISS, Version 3.2.1)



684  
 685

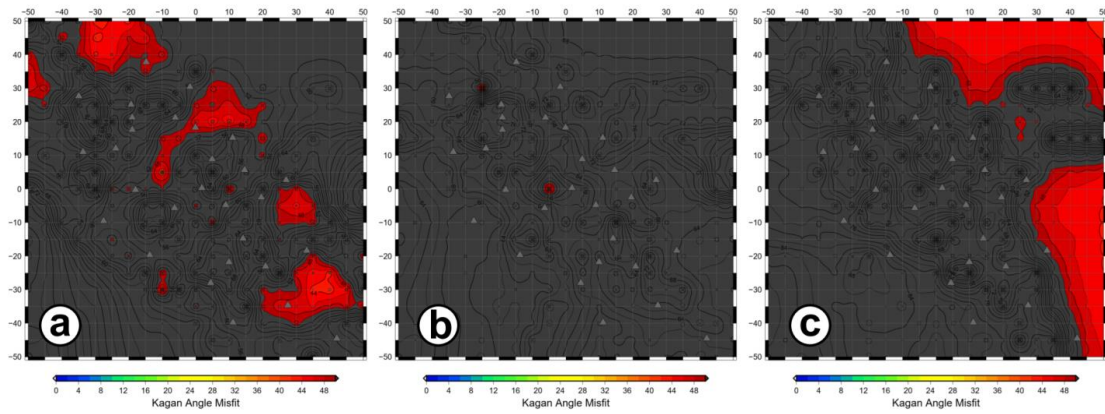
686 **Figure 2.** Fault plane solutions used for earthquake simulations. a) From left to right: 1) Ms 6.9, 23rd  
 687 November 1980 (FM1; Westaway ) 2) and 3) Median focal mechanism found from solutions from the  
 688 1<sup>st</sup> (FM2) and 5<sup>th</sup> (FM3) most populated bin of histogram of panel b. b) Fault plane solution classification  
 689 according to the plunge of P- and T-axes with specific tectonic regimes (Legend: NF, normal fault; NS,  
 690 normal-strike; SS, strike-slip; TF, thrust ; TS, thrust-strike; UF, unknown fault). The number of earthquakes  
 691 (color bar) is counted in bins of 15° × 15°.





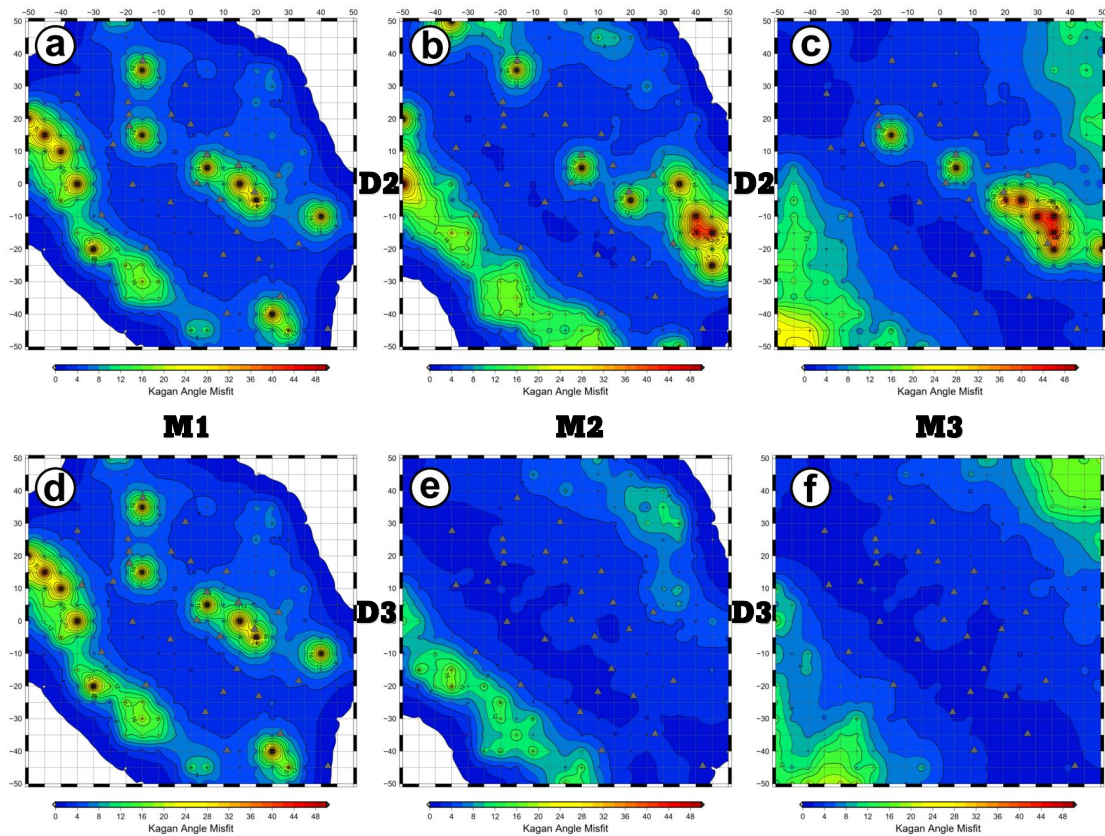
692  
693  
694  
695  
696  
697  
698  
699  
700  
701  
702  
703  
704  
705  
706

**Figure 3.** Regular grid of epicentres (yellow stars) used for simulating earthquakes. The area is 100x100 km<sup>2</sup> with 5 km of spacing along both horizontal coordinates. Irpinia Seismic Network (ISNet) is reported with red triangles.



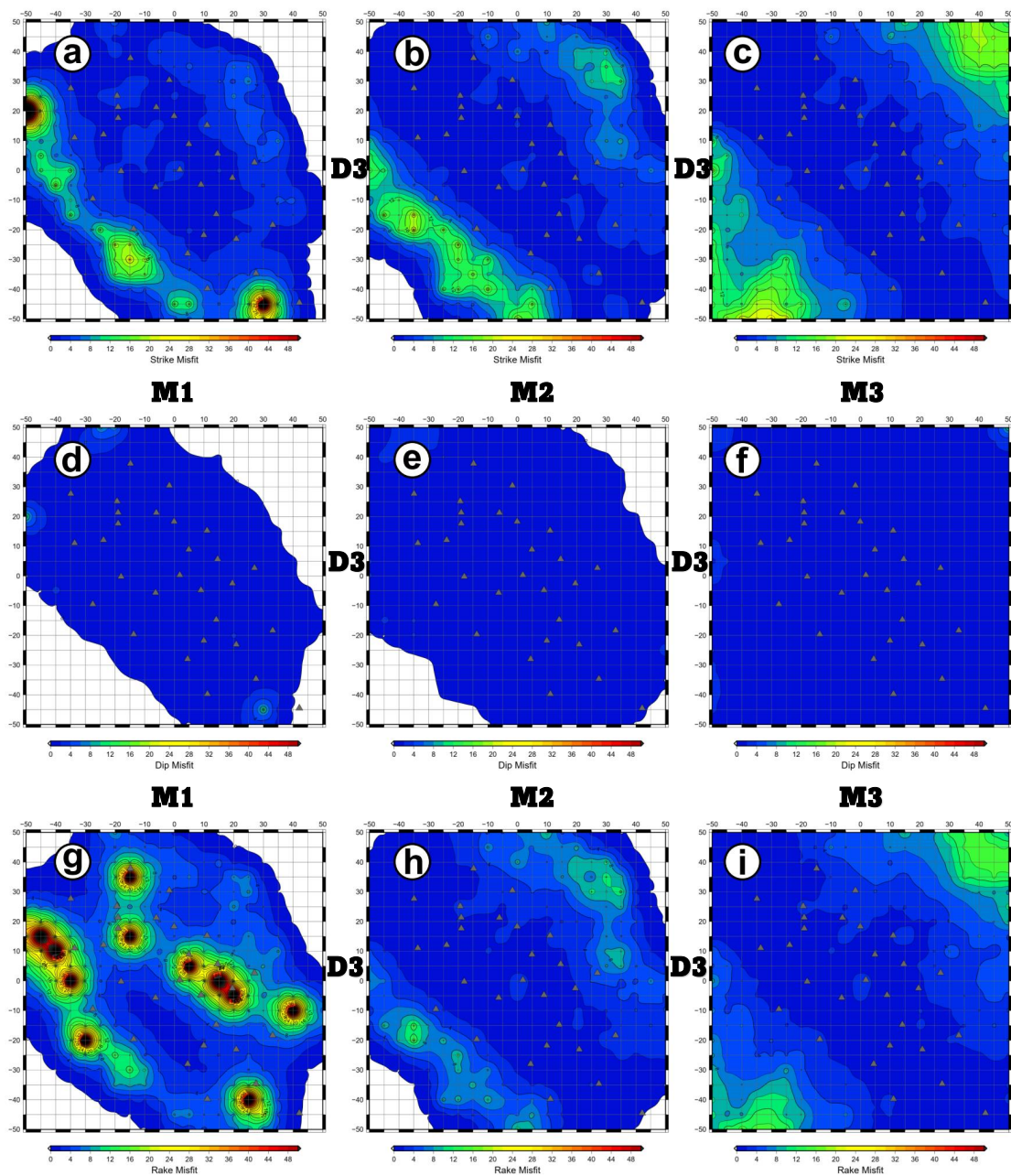
707  
708  
709  
710  
711  
712  
713  
714  
715  
716  
717  
718  
719  
720  
721  
722  
723  
724  
725  
726  
727  
728  
729  
730  
731  
732  
733  
734  
735  
736  
737

**Figure 4.** KAM (Kagan angle misfit) map for retrieved focal mechanisms with D1 dataset as input data and simulating earthquakes with M3 magnitude and FM1 (a), FM2 (b) and FM3 (c) theoretical fault plane solution at 10 km depth.



738  
739  
740  
741  
742  
743  
744  
745  
746  
747  
748

**Figure 5.** KAM (Kagan angle misfit) map for retrieved focal mechanisms with D2 (a, b, c) and D3 (d, e, f) datasets as input data and simulating earthquakes with M1 (a, d), M2 (b, e) and M3 (c, f) magnitudes and FM1 theoretical fault plane solution at 10 km depth. The level of gaussian noise is set to 5%.



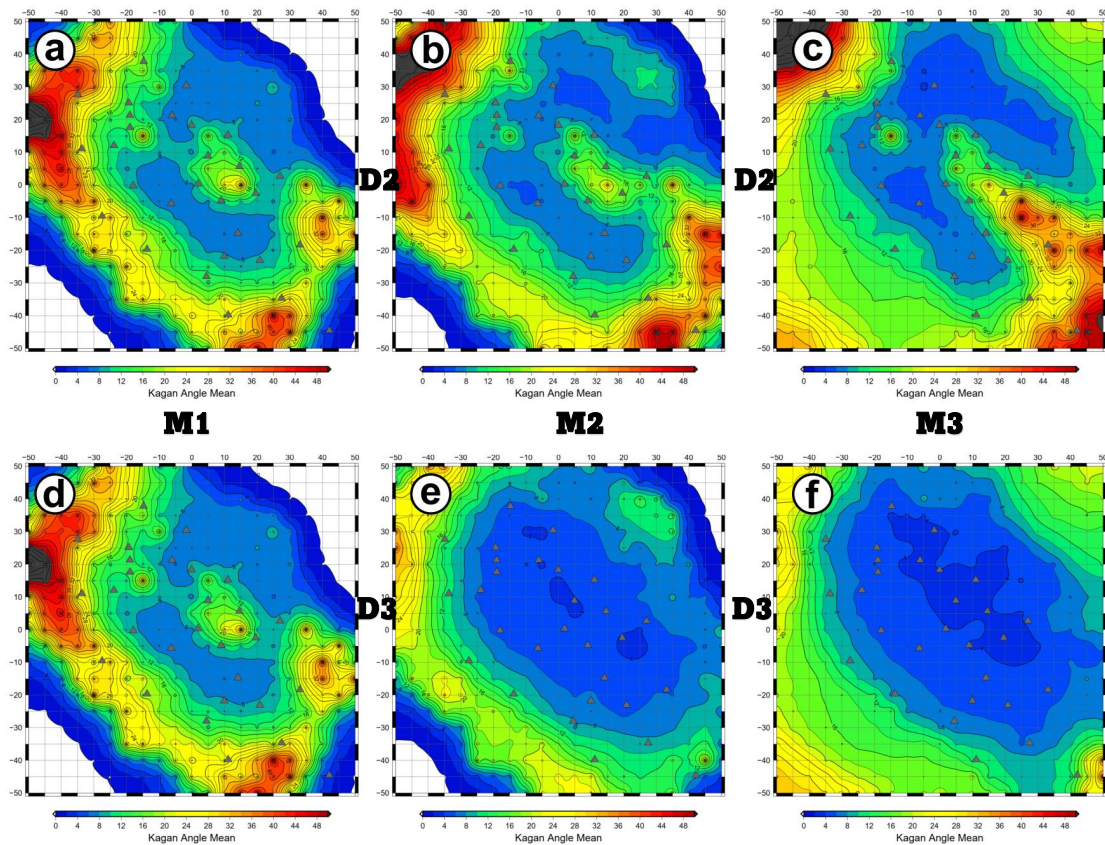
749  
750  
751  
752

**Figure 6.** FMM (focal mechanism parameter misfit) maps for retrieved focal mechanisms with D3 datasets as input data and simulating earthquakes with M1 (a, d, g), M2 (b, e, h) and M3 (c, f, i)



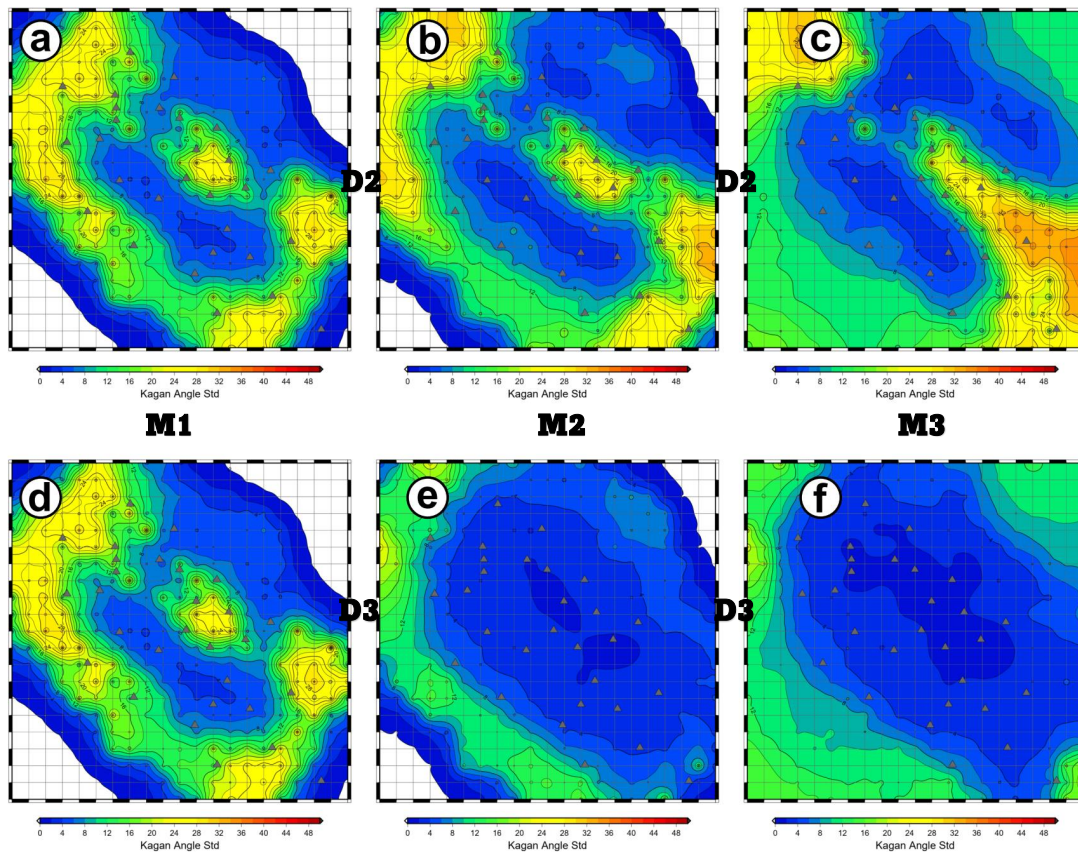
753 magnitudes and FM1 theoretical fault plane solution at 10 km depth. a, b, c refer to strike misfit; d, e,  
754 f refer to dip misfit; g, h, i refer to rake. The level of gaussian noise is set to 5%.

755  
756  
757  
758  
759  
760  
761  
762  
763  
764  
765  
766  
767  
768  
769  
770  
771  
772  
773  
774  
775  
776  
777  
778  
779  
780  
781  
782  
783  
784  
785  
786  
787  
788  
789  
790  
791  
792  
793  
794  
795  
796  
797  
798  
799  
800  
801



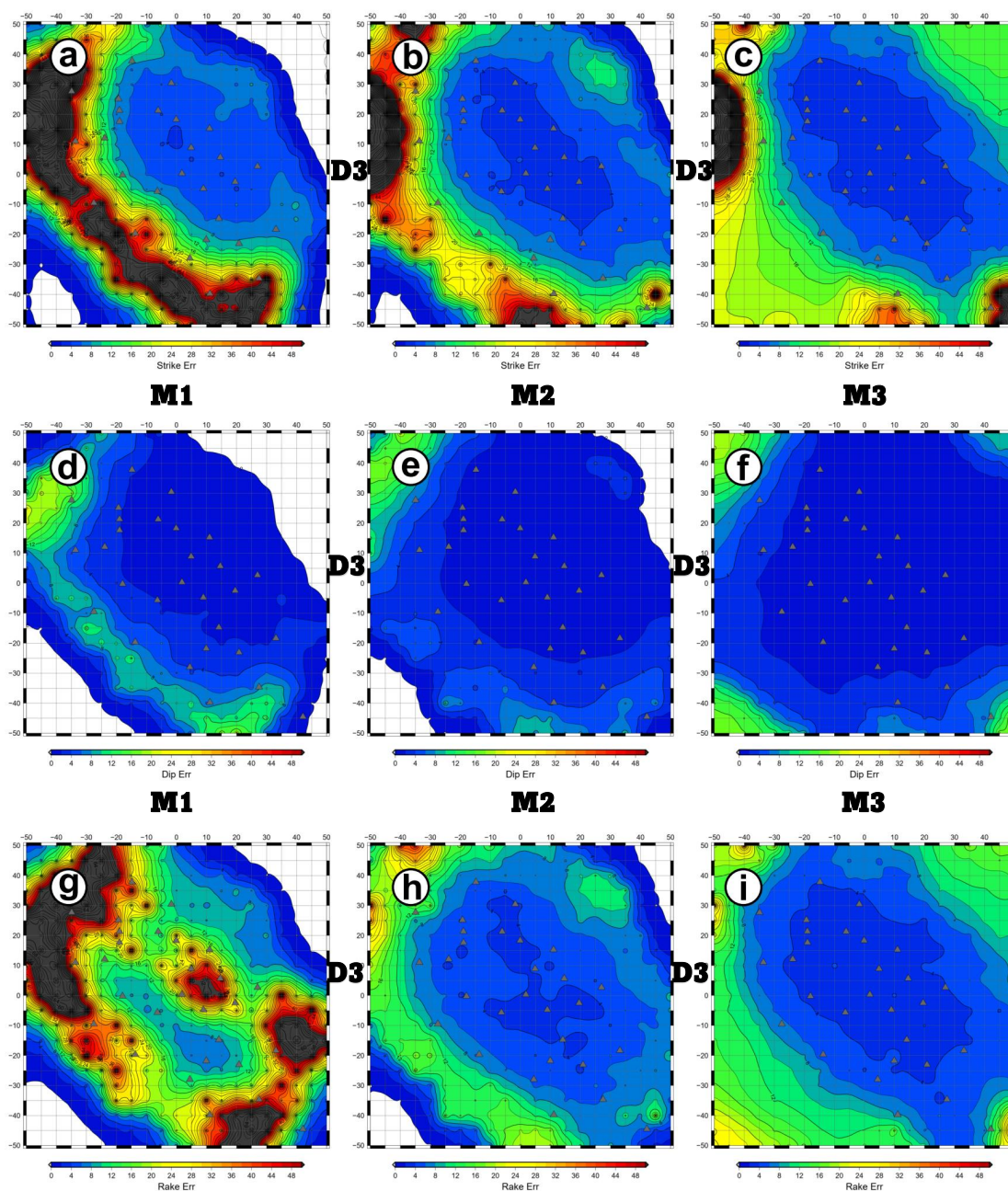
802  
803  
804  
805  
806  
807  
808  
809  
810  
811  
812  
813  
814  
815  
816  
817  
818

**Figure 7.** KAA (Kagan angle average) maps for retrieved focal mechanisms with D2 (a, b, c) and D3 (d, e, f) datasets as input data and simulating earthquakes with M1 (a, d), M2 (b, e) and M3 (c, f) magnitudes and FM1 theoretical fault plane solution at 10 km depth. The level of gaussian noise is set to 5%.



819  
820  
821  
822  
823  
824  
825  
826  
827  
828  
829  
830

**Figure 8.** KAS (Kagan angle standard deviation) maps for retrieved focal mechanisms with D2 (a, b, c) and D3 (d, e, f) datasets as input data and simulating earthquakes with M1 (a, d), M2 (b, e) and M3 (c, f) magnitudes and FM1 theoretical fault plane solution at 10 km depth. The level of gaussian noise is set to 5%.

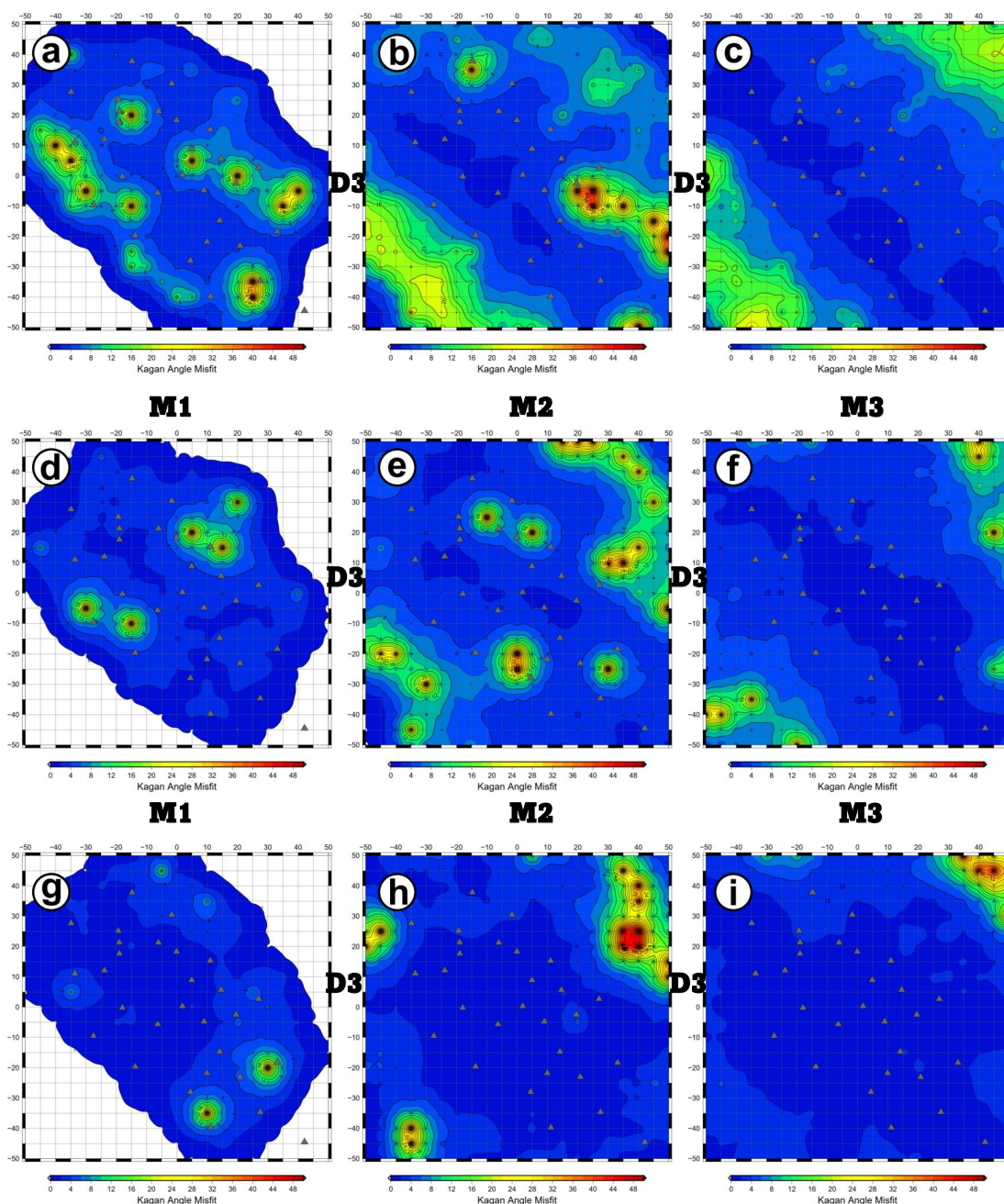


831  
832 **Figure 9.** FME (strike, dip and dake error) maps for retrieved focal mechanisms with D3 datasets as  
833 input data and simulating earthquakes with M1 (a, d, g), M2 (b, e, h) and M3 (c, f, i) magnitudes and





834 FM1 theoretical fault plane solution at 10 km depth. a, b, c refer to strike error; d, e, f refer to dip error;  
835 g, h, i refer to rake error. The level of gaussian noise is set to 5%.  
836

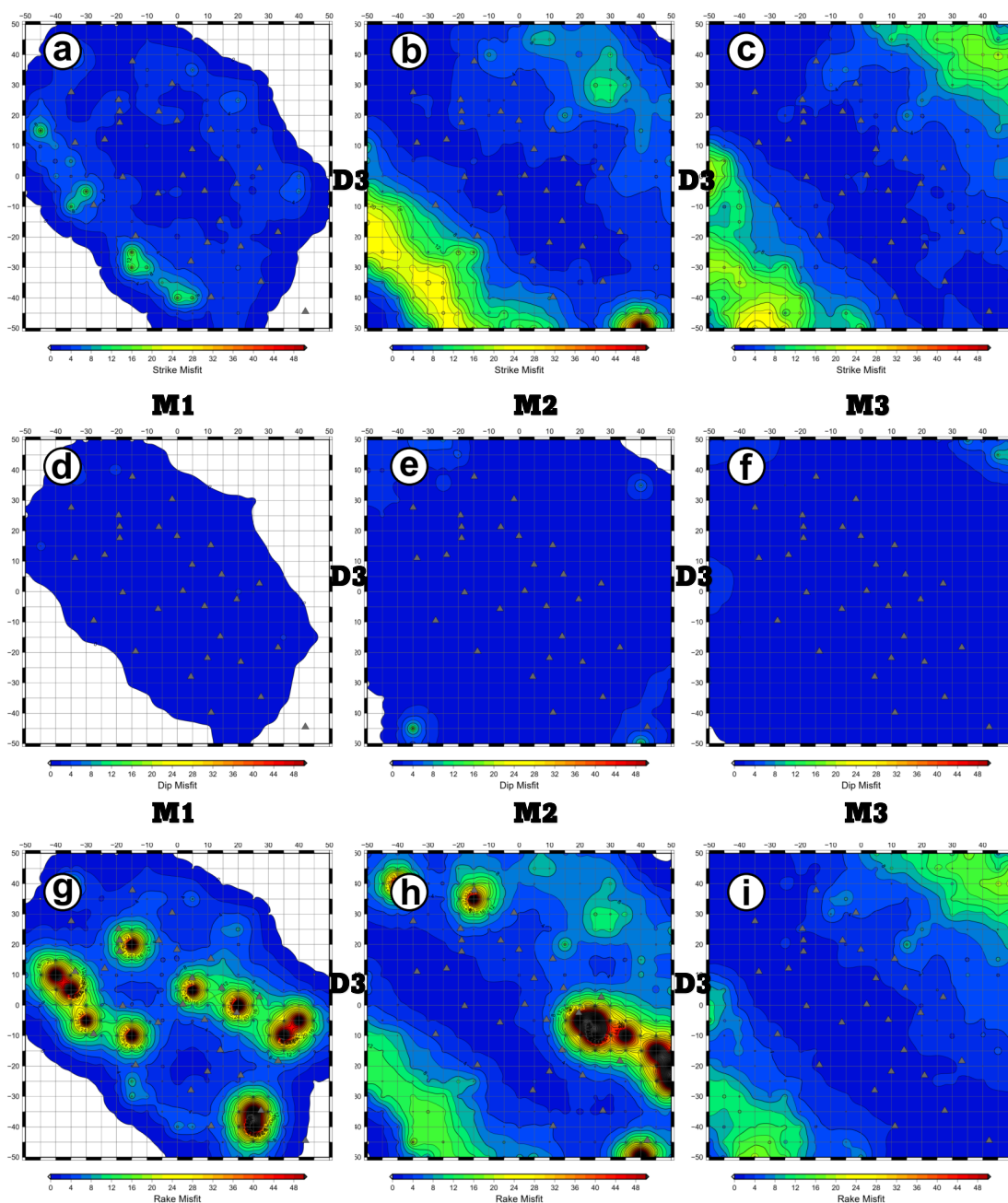


837

838 **Figure 10.** KAM (Kagan angle misfit) maps for retrieved focal mechanisms with D3 datasets as input  
839 data and simulating earthquakes with M1 (a, d, g), M2 (b, e, h) and M3 (c, f, i) magnitudes and FM1 (a,



840 b, c), FM2 (d, e, f) and FM3 (g, h, i) theoretical fault plane solution at 10 km depth. The level of  
841 gaussian noise is set to 5%.  
842

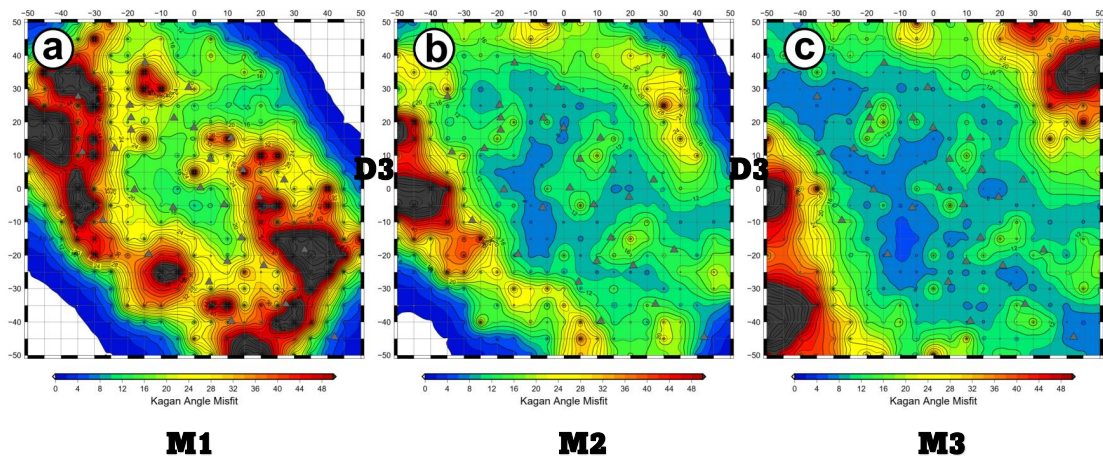


843  
844 **Figure 11.** FMM (focal mechanism parameter misfit) maps for retrieved focal mechanisms with D3  
845 datasets as input data and simulating earthquakes with M1 (a, d, g), M2 (b, e, h) and M3 (c, f, i)



846 magnitudes and FM1 theoretical fault plane solution at 5 km depth. a, b, c refer to strike misfit; d, e, f  
847 refer to dip misfit; g, h, i refer to rake. The level of gaussian noise is set to 5%.

848  
849  
850  
851  
852  
853  
854  
855  
856  
857  
858  
859  
860  
861  
862  
863  
864  
865  
866  
867  
868  
869  
870  
871  
872  
873  
874  
875  
876  
877  
878  
879  
880



881  
882 **Figure 12.** KAM (Kagan angle misfit) map for retrieved focal mechanisms with D3 (a, b, c) datasets as  
883 input data and simulating earthquakes with M1 (a), M2 (b) and M3 (c) magnitudes and FM1 theoretical  
884 fault plane solution at 10 km depth. The level of gaussian noise is set to 30%.

885  
886  
887  
888  
889  
890  
891  
892  
893  
894  
895  
896  
897  
898  
899  
900  
901  
902  
903  
904  
905  
906  
907  
908  
909  
910  
911  
912